energies

MDPI

Article

Evaluation of Rail Potential Based on Power Distribution in DC Traction Power Systems

Guifu Du, Dongliang Zhang *, Guoxin Li, Chonglin Wang and Jianhua Liu

School of Information and Electrical Engineering, China University of Mining and Technology, Xuzhou 221008, China; cumt_dgf@126.com (G.D.); lee_guoxin@126.com (G.L.); chlwang@cumt.edu.cn (C.W.); ljh5605@126.com (J.L.)

* Correspondence: zdl@cumt.edu.cn; Tel.: +86-516-8388-5605

Academic Editor: Paul Stewart

Received: 8 July 2016; Accepted: 5 September 2016; Published: 9 September 2016

Abstract: Running rails used as a return conductor and ungrounded scheme have been widely adopted in DC traction power systems. Due to the longitudinal resistance of running rails and insulation resistance of rail-to-ground, there will be a potential rise between running rails and the ground when return current flows through the running rails, which is known as rail potential. At present, abnormal rise of rail potential exists widely in DC traction power systems. The present rail potential model still cannot simulate and explain the abnormal rail potential in the system. Based on the analysis of power distribution with multiple trains running in multiple sections, a dynamic simulation model of rail potential in the whole line is proposed. The dynamic distribution of rail potential and stray current in DC traction power systems when multiple trains run in multiple sections is analyzed, and the impact of traction current distribution on rail potential is evaluated. Simulation results show that the abnormal rise of rail potential during the dynamic operation of the system can be evaluated effectively.

Keywords: DC traction power systems; rail potential; power distribution; stray current

1. Introduction

Direct current (DC) traction power systems with an ungrounded scheme are widely used in urban rail transit lines; the running rails are usually used as return conductor. Due to the longitudinal resistance of running rails, there will be a potential between running rails and the ground when traction current flows back to the traction substation, which is called rail potential. Since the running rails cannot be completely insulated to the ground, some of the return current will leak from running rails into the ground and buried metallic structures, which is known as stray current [1]. At present, abnormal rise of rail potential and stray current exists in many urban railway lines, which may exceed the limit value stipulated in relative standards [2,3]. This will cause damage to human safety and electrochemical corrosion of reinforcing bars and buried metal pipelines [4,5]. In order to guarantee human safety and normal operation of equipment, the regulations to control the rail potential in DC traction power systems should be designed [6,7]. Maximum permissible body voltages as a function of time duration in DC traction systems are provided in IEC 62128-1 [3]. For long-term conditions, the accessible rail potential shall not exceed 120 V. Voltage-limiting devices are usually used to reduce the rail potential by connecting the running rails to the substation ground, in which case the current leakage from voltage-limiting devices can reach 800 A, and the stray current increases significantly. Currently, abnormal rise of rail potential cannot be simulated and evaluated by existing models when multiple trains run in multiple sections. Many anomalies in the line cannot be clarified. For example, rail potential in the first and last sections is much higher than that in the middle sections during the operation of the line. In many lines, rail potential in the first and last sections frequently

surpasses the stipulated limits [8]. Although the longitudinal resistance of running rails meets the design requirements, rail potential is still high and inconsistent with the theoretical calculation results. Therefore, the dynamic distribution of rail potential needs further studying when multiple trains run in multiple sections.

There are some studies on controlling the rail potential in DC traction power systems. Relevant studies show that [9,10] reducing the resistance of running rails, improving the voltage level of power supply systems and shortening the distance between traction substations can drop the rail potential effectively. In addition, different grounding schemes of the system—such as solid grounding, diode grounding and being ungrounded—have an impact on rail potential distribution [10]. A number of simulations and experimental results [9] show that the connecting cables between different railway lines are the main cause of high rail potential. What is more, running modes of trains [11], cross-track regeneration supply [12] and other factors also influence the distribution of rail potential and stray current. However, the impact of power distribution on rail potential when multiple trains run in multiple sections has broadly been ignored, and the abnormal rise of rail potential in the actual line has not yet been clarified.

In the last few decades, the simulation model of rail potential and stray current have been studied. The distribution of rail potential is analyzed through finite-element methods and distributed parameter model of return circuit [12–14]. Charalambous [12] uses CDEGS software from Safe Engineering Services & Technologies, Ltd. (SES) in Canada to analyze and assess the change of stray current when the cross-track regeneration supply exists. Meanwhile, a topologically accurate model in cut-and-cover sections of DC traction power systems is established to simulate the dynamic distribution of stray current under the influence of train characteristics, time tabling, headway, etc. [13]. In a lumped parameter model of rail potential and stray current [9,14], a segment of 100 m is sufficient and accurate for the simulation, but the conductance matrixes of the whole line will be very large, and speed of the calculation will be slow. In a distributed parameter model of rail potential and stray current [11,15], the impact of power distribution between source nodes and load nodes on rail potential is always ignored. Traction current transmitting over sections exists widely when multiple trains run in multiple sections in DC traction power systems. As stated by Lin [16] and Falvo [17], in DC traction power systems, all traction substations and trains are in parallel operation for the connectivity of the catenary and running rails in the whole line. Traction current of an accelerating train comes not only from the traction substations of the section, but also from traction substations in other sections or regenerative braking trains with a long distance. The current that regenerative braking trains feed back to the catenary can supply power for accelerating trains in other sections. However, little attention has been paid to the power distribution between source nodes and load nodes. Traction current transmitting with a long distance will have an impact on rail potential. The number of nodes in the network of DC traction power systems is large, and the running mode of the traction substation and train can change, becoming very complicated. Subsequently, current flow has many paths. The current distribution between power source nodes and load nodes cannot be drawn exactly by power flow calculation. When multiple trains run in multiple sections, traction current distribution is affected by the parameters of rectifier units, the train's running modes, as well as the coincidence degree of the trains, parameters of regenerative braking energy absorbing device (RBEAD), line parameters, etc. At present, related l studies [18,19] generally focus on the method of power flow calculation, whereas little attention has been paid to the power flow tracing in a DC traction power system with multiple nodes. Traction current distribution relations between source nodes and load nodes need to be calculated. The impact of traction current distribution on an abnormal rise of rail potential when multiple trains run dynamically in multiple sections is lack of accurate modeling and analysis. For the realization of fast and accurate calculation of rail potential, a new simulation model is proposed in this paper. The simulation model of rail potential consists of the train movement calculation module, power flow calculation module, power flow tracing calculation module and rail potential calculation module.

This paper illustrates the impact of power distribution on rail potential. A dynamic model of rail potential based on power distribution when multiple trains run in multiple sections is established, thereby clarifying the abnormal rise of rail potential in the actual line. Field tests and simulations show that traction current transferring over sections widely exists in DC traction power systems, and the abnormal rise of rail potential during the dynamic operation of the system can be evaluated effectively.

2. System Description

A DC traction power system mainly consists of rectifier units, catenaries, trains, running rails, buried conductor, RBEAD, etc. A schematic of a DC traction power system is shown in Figure 1. For the connectivity of catenaries and running rails in the whole line, all the trains and traction substations are in parallel operation.

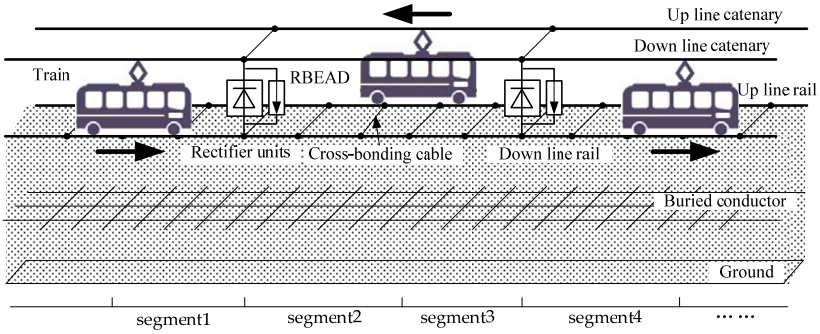

Figure 1. Schematic of DC traction power system.

The 24-pulse diode rectifier units are usually set in traction substations, which can provide unidirectional current from the alternating current (AC) side to DC side. In this paper, assuming that internal resistance of the rectifier units is changeless, output characteristic of the rectifier units is shown as line I in Figure 2. A train's running mode can actually be divided into three stages: accelerating, coasting and braking. Regenerative braking is the main braking method, which will feed the current back to the catenary and rise catenary voltage. When the catenary voltage rises to no-load voltage, U_0, of the rectifier units, rectifier units will be out of operation. The output characteristic is shown as line II in Figure 2. If the current that regenerative braking trains feed back to the catenary cannot be fully absorbed by surrounding accelerating trains, then catenary voltage will rise continuously. In order to prevent the catenary voltage from exceeding the safety limit, an RBEAD is usually set in trains or traction substations. When the catenary voltage at RBEAD exceeds its trigger voltage, U_{max}, the RBEAD will start to absorb the remaining energy so as to ensure that the catenary voltage does not exceed U_{max}. In the urban railway lines of China, the RBEAD is usually set at traction substations, and its output characteristic is shown as line III in Figure 2. The output characteristic of traction substation with RBEAD is shown in Figure 2.

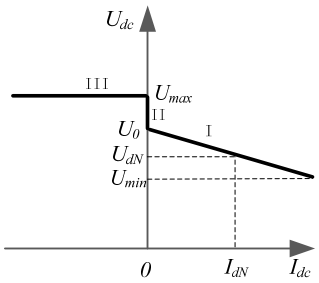

Figure 2. Output characteristic of traction substation with regenerative braking energy absorbing device (RBEAD).

The train's traction and regenerative braking curve are constrained by the traction network voltage. With the drop of traction network voltage, train tractive and regenerative braking capacity will be limited [16]. In this paper, the models are simplified without considering the effect of traction network voltage on train traction and braking performance, and it is assumed that the current network voltage can meet the needs of the train traction and braking performance. In the dynamic operation of DC traction power systems, the voltage and current at each node of traction substation or train can be obtained by power flow calculation at each moment. At present, there are many pieces of power flow calculation software for DC traction power systems to obtain the current and voltage at each node [20,21]. Power flow calculation software for DC traction power systems mainly consists of a train movement calculation model and power flow calculation model. With the route parameters, train characteristics, and scheduled timetables, etc., the relation between power and time, as well as the relation between position and time of the trains, can be obtained by the train movement calculation model. Then, parameters such as the current, voltage and power of traction substations and trains at each moment can be attained through the power flow calculation model.

As shown in Figure 1, the return circuit consists of running rails, the buried conductor and the ground. Up line rail and down line rail are connected by cross-bonding cables at intervals of 400 m∼500 m. The buried conductor is set in the ballast bed to collect stray current. The distributed parameters of the return circuit must be converted to lumped parameters for the calculation of power flow. For the realization of fast and accurate calculation of rail potential in this paper, the segment of return circuit between traction substation and train is converted to double π circuit in the power flow calculation. In order to ensure the accuracy of the lumped parameters in double π circuit, the parameters can be calculated by the distributed parameter model [22]. The model in power flow calculation is shown in Figure 3.

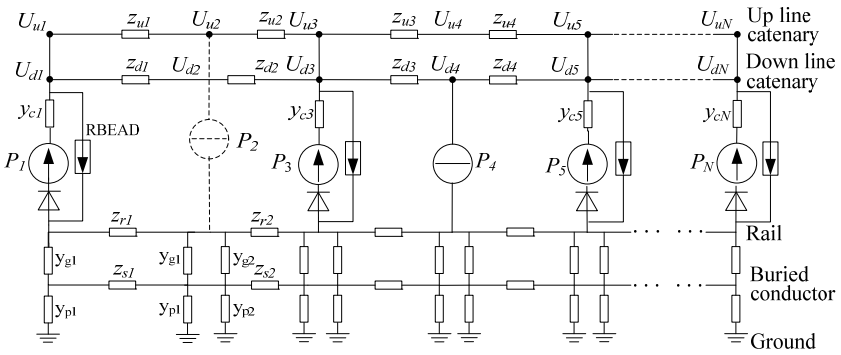

Figure 3. Lumped parameter model in power flow calculation.

As shown in Figure 3, the train is equivalent to a constant power model in the up line or down line, such as P_2 and P_4. P_2 and P_4 are the power of trains at this moment. y_{cN} is the equivalent resistance of the traction substation. z_{r1} and z_{s1} are the equivalent resistances of the rail and the buried conductor. y_{g1} is the equivalent conductance of rail to buried conductor. y_{p1} is the equivalent conductance of buried conductor to the ground. Based on the lumped parameter model at each moment shown in Figure 3, the nodal voltage equations can be obtained, and the power flow can be calculated by iterative methods.

For the realization of fast and accurate calculation of the rail potential, the return circuit between traction substation and train is converted to lumped parameters in the power flow calculation. In order to obtain the rail potential and stray current at each position and evaluate the impact of power distribution on rail potential, the power flow tracing of the system should be calculated, and the rail potential should be calculated by the distributed parameter model of the return circuit.

3. Power Flow Tracing of DC Traction Power Systems

When multiple trains run in multiple sections, the current of each node and branch can be drawn based on power flow calculation at a certain moment. However, it is difficult to obtain the traction current distribution between source nodes and load nodes due to the complexity of the current flow path. The source nodes and load nodes on the catenary at one moment are shown in Figure 4. The current that the regenerative braking train at node 14 feeds back to the catenary can flow to node 7. However, due to the complexity of the path and nodes, it is difficult to calculate the current distribution between nodes 14 and 7. Therefore, it is necessary to trace the power flow in order to obtain the traction current distribution coefficients between the source nodes and the load nodes.

Assuming that there are N nodes on the line at a moment, the traction current distribution coefficient k_{ij} from the current of source node i, I_{Gi}, to current of load node j, I_{Lj}, is shown in Equation (1):

$$I_{ij} = k_{ij} I_{Lj} \tag{1}$$

I_{ij} is the current from source node i to load node j. The traction current distribution coefficient $\boldsymbol{K}$ of all source nodes and all load nodes is calculated based on the power flow tracing of the DC traction power system.

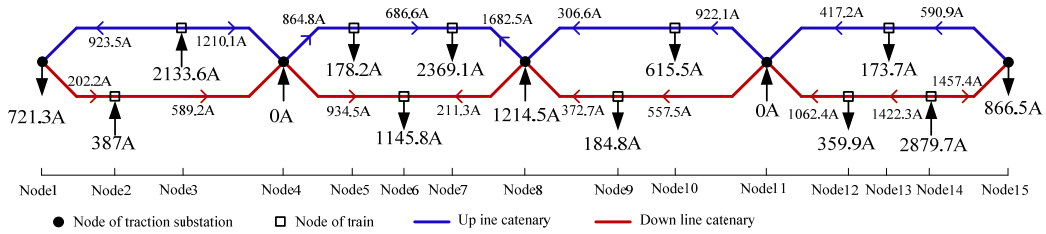

Figure 4. Source nodes and load nodes on the catenary at one moment.

An analytic model of current distribution in a DC traction power system is established in this paper. In this way, the current distribution relation can be accurately calculated between the power sources and the loads in order to obtain the current and power supply areas.

Assuming that $\boldsymbol{A} = (a_{ij})_{N\times N}$ is the downstream distribution matrix of a power network with N nodes and I_{ij} is the current supply from node i to node j by i-j branch, the downstream distribution matrix can be expressed as follows:

$$a_{ij} = \begin{cases} -I_{ij}/I_{Tj}, & i \neq j, I_{ij} > 0 \\ 1, & i = j \\ 0, & else \end{cases} \tag{2}$$

where, $i, j = 1, 2, 3, \ldots, N$. I_{Tj} is the total injected current of node j.

As shown in Equation (2), the downstream distribution matrix includes the connection relationship between nodes, current flows in branches and the injected current values. The downstream distribution matrix is an unsymmetrical matrix.

$\boldsymbol{I}_L = [I_{L1}, I_{L2}, \ldots, I_{LN}]^T$, $\boldsymbol{I}_G = [I_{G1}, I_{G2}, \ldots, I_{GN}]^T$ and $\boldsymbol{I}_T = [I_{T1}, I_{T2}, \ldots, I_{TN}]^T$ respectively represent the N-dimension load current column vector, source current column vector and total injected

current column vector. Based on Kirchhoff's current law, the input current of each node is equal to the output current, so the vector $\boldsymbol{I}_L$ and $\boldsymbol{A}\boldsymbol{I}_T$ can be expressed as:

$$\begin{aligned} \sum_{j=1}^{N} a_{ij} I_{Tj} &= I_{Ti} + \sum_{j=1, j\neq i, I_{ij}>0}^{N} \left(\frac{-I_{ij}}{I_{Tj}}\right) I_{Tj} \\ &= I_{Ti} - \sum_{j=1, j\neq i, I_{ij}>0}^{N} I_{ij} = I_{Li} \end{aligned} \tag{3}$$

where, $i = 1, 2, \ldots, N$.

It can be expressed as:

$$\boldsymbol{A}\boldsymbol{I}_T = \boldsymbol{I}_L \tag{4}$$

$\boldsymbol{I}_{LL} = diag(I_{L1}, I_{L2}, \ldots, I_{LN})$, $\boldsymbol{I}_{GG} = diag(I_{G1}, I_{G2}, \ldots, I_{GN})$ and $\boldsymbol{I}_{TT} = diag(I_{T1}, I_{T2}, \ldots, I_{TN})$ are the $N \times N$ diagonal matrix, $\boldsymbol{E} = [1, 1, \ldots, 1]^T$ is the N-dimension unit column vector. The relation of $\boldsymbol{I}_T$ and $\boldsymbol{I}_{TT}$ can be expressed as Equation (5), and the relation of $\boldsymbol{I}_G$ and $\boldsymbol{I}_{GG}$ can be expressed as Equation (6).

$$\boldsymbol{I}_T = [I_{T1}, I_{T2}, \ldots, I_{TN}]^T = \boldsymbol{I}_{TT}\boldsymbol{E} \tag{5}$$

$$\boldsymbol{I}_G = [I_{G1}, I_{G2}, \ldots, I_{GN}]^T = \boldsymbol{I}_{GG}\boldsymbol{E} \tag{6}$$

The analytic relation between $\boldsymbol{I}_G$ and $\boldsymbol{I}_L$ can be expressed as Equation (7).

$$\boldsymbol{I}_G = \boldsymbol{I}_{GG}\boldsymbol{E} = \boldsymbol{I}_{GG}\left(\boldsymbol{I}_{TT}\right)^{-1}\boldsymbol{I}_T = \boldsymbol{I}_{GG}\left(\boldsymbol{I}_{TT}\right)^{-1}\boldsymbol{A}^{-1}\boldsymbol{I}_L \tag{7}$$

That is,

$$\boldsymbol{I}_G = \boldsymbol{I}_{GG}(\boldsymbol{I}_{TT})^{-1}\boldsymbol{A}^{-1}\boldsymbol{I}_L \tag{8}$$

The current distribution between power sources and loads is presented in Equation (8). $\boldsymbol{I}_{GG}(\boldsymbol{I}_{TT})^{-1}\boldsymbol{A}^{-1}$ is the traction current distribution coefficients. $\boldsymbol{K} = (k_{ij})$, then,

$$\boldsymbol{K} = \boldsymbol{I}_{GG}(\boldsymbol{I}_{TT})^{-1}\boldsymbol{A}^{-1} \tag{9}$$

So,

$$I_{Gi} = \sum_{j=1}^{N} k_{ij} I_{Lj} \tag{10}$$

where, $I_{ij} = k_{ij} I_{Lj}$ is the current that the power source at node i supplies for the load at node j.

Based on the current distribution principle, the sum of current distribution coefficients of each power source to all loads should be 1.

The matrix of traction current distribution coefficients meet the relation presented in Equation (11):

$$\boldsymbol{E}^T\boldsymbol{K} = \boldsymbol{E}^T\boldsymbol{I}_{GG}\boldsymbol{I}_{TT}^{-1}\boldsymbol{A}^{-1} = \left(\boldsymbol{I}_G\right)^T\left(\boldsymbol{A}\boldsymbol{I}_{TT}\right)^{-1} \tag{11}$$

In order to obtain the property of $\boldsymbol{K}$, the relation between $\left(\boldsymbol{I}_G\right)^T$ and $\boldsymbol{A}\mathbf{I}_{TT}$ should be solved.

Assuming that $\boldsymbol{B} = \boldsymbol{A}\boldsymbol{I}_{TT}$, the element at i-th row and j-th column is:

$$B_{ij} = \begin{pmatrix} a_{i1} & a_{i2} & \ldots & a_{iN} \end{pmatrix} \begin{bmatrix} \left(\boldsymbol{I}_{TT}\right)_{1j} \\ \left(\boldsymbol{I}_{TT}\right)_{2j} \\ \ldots \\ \left(\boldsymbol{I}_{TT}\right)_{Nj} \end{bmatrix} \tag{12}$$

$\boldsymbol{I}_{TT}$ is a diagonal matrix. Based on $\boldsymbol{I}_{TT}$ and $\boldsymbol{I}_T$, $B_{ij} = a_{ij}B_{jj} = a_{ij}I_{Tj}$. Based on Equation (2), we can deduce that:

$$B_{ij} = \begin{cases} -I_{ij}, & i \neq j, I_{ij} > 0 \\ I_{Tj}, & i = j \\ 0, & else \end{cases} \tag{13}$$

Therefore, the sum of elements in j-th column of matrix $\boldsymbol{B}$ is:

$$\sum_{i=1}^{N} B_{ij} = \sum_{s=1}^{j-1} B_{sj} + B_{jj} + \sum_{s=j+1}^{N} B_{sj} \tag{14}$$

By the definition of B_{ij} and I_{Tj}, we can know that:

$$\sum_{i=1}^{N} B_{ij} = \sum_{s=1}^{j-1} B_{sj} + I_{Gj} + \sum_{i,I_{ij}>0} I_{ij} + \sum_{s=j+1}^{N} B_{sj} = I_{Gj} \tag{15}$$

That is:

$$(\boldsymbol{I}_G)^T = \boldsymbol{E}^T \boldsymbol{A} \boldsymbol{I}_{TT} \tag{16}$$

Then, $\boldsymbol{E}^T \boldsymbol{K} = \boldsymbol{E}^T \boldsymbol{I}_{GG} \boldsymbol{I}_{TT}^{-1} \boldsymbol{A}^{-1} = (\boldsymbol{I}_G)^T (\boldsymbol{A}\boldsymbol{I}_{TT})^{-1} = \boldsymbol{E}^T$, and the sum of each column element is 1, which complies with the current distribution principle.

Based on the above method, the current distribution of all power sources and loads at a moment can be obtained in DC traction power systems.

4. Modeling of Rail Potential

In DC traction power systems, multiple trains run in multiple sections. The current at load node comes from many power sources, and each power source supplies power to many load nodes simultaneously. On the basis of traction current distribution coefficients, the line consists of multiple power supply sections. The return circuit is a linear model, and it follows linear superposition theorem. The rail potential with multiple trains running in multiple sections can be obtained by superimposing the rail potential of each power supply section in the line, assuming that the total length of the line is L and there are N nodes in the line. The direction of 0 to L is the positive value of current in running rails. The positive current of the traction substation and train indicates that the current is injected to the rail. The power supply section from j-th source node to i-th load node is shown in Figure 5a. The traction current that I_{Gj} supplies for I_{Li} is $I_{ji} = k_{ji}I_{Gj}$, the position of j-th source node is x_j and the position of i-th load node is x_i.

Assuming that a single power supply section exists in x_i to x_j, and the supply current is $k_{ji}I_{Gj}$, then the rail potential in the line is divided into three continuous change sections. The distributed parameter model of the return circuit at any point between x to $(x + dx)$ is shown in Figure 5b.

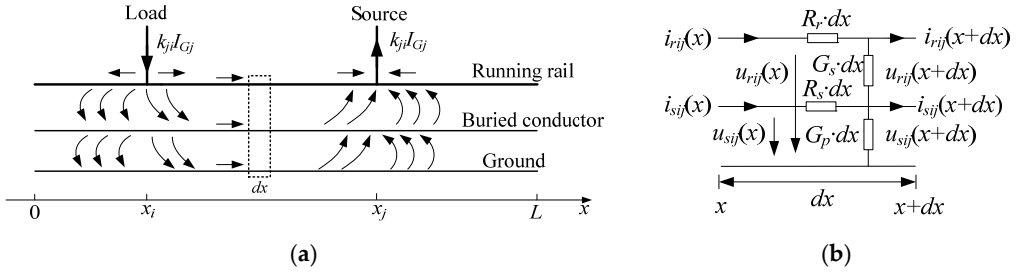

Figure 5. Return circuit model with a power supply section, (**a**) A power supply section exists in the line; (**b**) The model of the return circuit in dx.

As shown in Figure 5b, $u_{rij}(x)$, $u_{sij}(x)$, $i_{rij}(x)$ and $i_{sij}(x)$ respectively represent rail potential, potential of buried conductor to the ground, current in rail and stray current in buried conductor at position x. Based on Kirchhoff's law, these parameters meet the following equation:

$$\begin{cases} \frac{du_{rij}(x)}{dx} = -R_r \cdot i_{rij}(x) \\ \frac{du_{sij}(x)}{dx} = -R_s \cdot i_{sij}(x) \\ \frac{di_{rij}(x)}{dx} = -G_s \cdot u_{rij}(x) + G_s \cdot u_{sij}(x) \\ \frac{di_{sij}(x)}{dx} = G_s \cdot u_{rij}(x) - (G_p + G_s) \cdot u_{sij}(x) \end{cases} \tag{17}$$

where, R_r is the longitudinal resistance of the running rail, Ω/km; R_s is the longitudinal resistance of the buried conductor, Ω/km; G_s is the longitudinal insulation conductance of rails to the buried conductor, S/km; G_p is the longitudinal insulation conductance of the buried conductor to the ground, S/km.

Due to the different boundary conditions of three sections, the undetermined coefficient of rail potential is different in the three sections.

The parameters in section 0 to x_i can be expressed as follows:

$$\begin{bmatrix} u_{rij1}(x) \\ u_{sij1}(x) \\ i_{rij1}(x) \\ i_{sij1}(x) \end{bmatrix} = \boldsymbol{H} \times \begin{bmatrix} C_{ij1}e^{-\alpha x} \\ C_{ij2}e^{\alpha x} \\ C_{ij3}e^{-\beta x} \\ C_{ij4}e^{\beta x} \end{bmatrix}, \ 0 \le x < x_i \tag{18}$$

The parameters in section x_i to x_j can be expressed as follows:

$$\begin{bmatrix} u_{rij2}(x) \\ u_{sij2}(x) \\ i_{rij2}(x) \\ i_{sij2}(x) \end{bmatrix} = \boldsymbol{H} \times \begin{bmatrix} C_{ij5}e^{-\alpha x} \\ C_{ij6}e^{\alpha x} \\ C_{ij7}e^{-\beta x} \\ C_{ij8}e^{\beta x} \end{bmatrix}, \ x_i \le x < x_j \tag{19}$$

The parameters in section x_j to L can be expressed as follows:

$$\begin{bmatrix} u_{rij3}(x) \\ u_{sij3}(x) \\ i_{rij3}(x) \\ i_{sij3}(x) \end{bmatrix} = \boldsymbol{H} \times \begin{bmatrix} C_{ij9}e^{-\alpha x} \\ C_{ij10}e^{\alpha x} \\ C_{ij11}e^{-\beta x} \\ C_{ij12}e^{\beta x} \end{bmatrix}, \ x_j \le x \le L \tag{20}$$

where, $\boldsymbol{H} = \begin{bmatrix} 1 & 1 & 1 & 1 \\ 1 - \frac{\alpha^2}{G_s R_r} & 1 - \frac{\alpha^2}{G_s R_r} & 1 - \frac{\beta^2}{G_s R_r} & 1 - \frac{\beta^2}{G_s R_r} \\ \frac{\alpha}{R_r} & -\frac{\alpha}{R_r} & \frac{\beta}{R_r} & -\frac{\beta}{R_r} \\ r_\alpha & -r_\alpha & r_\beta & -r_\beta \end{bmatrix}$, $r_\alpha = \frac{G_p}{\alpha} - \frac{\alpha}{R_r} - \frac{G_p \alpha}{G_s R_r}$, $r_\beta = \frac{G_p}{\beta} - \frac{\beta}{R_r} - \frac{G_p \beta}{G_s R_r}$, $\alpha = \sqrt{\frac{m+n}{2} + \sqrt{\frac{(m-n)^2}{4} + mk}}$, $\beta = \sqrt{\frac{m+n}{2} - \sqrt{\frac{(m-n)^2}{4} + mk}}$, $m = G_s R_r$, $n = R_s(G_s + G_p)$, and $k = R_s G_s$. C_{ij1}~C_{ij12} are the undetermined coefficients that can be obtained by the boundary conditions in each section.

C_{ij1}~C_{ij12} can be obtained by Equation (21) as follows:

$$\begin{cases} i_{rij1}(0) = 0 \\ -i_{rij1}(x_i) + i_{rij2}(x_i) = k_{ji} I_{Gj} \\ u_{rij1}(x_i) = u_{rij2}(x_i) \\ i_{rij2}(x_j) - i_{rij3}(x_j) = k_{ji} I_{Gj} \\ u_{rij2}(x_j) = u_{rij3}(x_j) \\ i_{rij3}(L) = 0 \\ i_{sij1}(0) = 0 \\ i_{sij1}(x_i) = i_{sij2}(x_i) \\ u_{sij1}(x_i) = u_{sij2}(x_i) \\ i_{sij2}(x_j) = i_{sij3}(x_j) \\ u_{sij2}(x_j) = u_{sij3}(x_j) \\ i_{sij3}(L) = 0 \end{cases} \tag{21}$$

Then, the $u_{rij}(x)$, $u_{sij}(x)$, $i_{rij}(x)$ and $i_{sij}(x)$ can be obtained when a power supply section from x_i to x_j exists in the line.

There may be up to $N \times N$ power supply sections in the line, and the return circuit is a linear model, which meets the linear superposition theorem. At a certain time, the rail potential with multiple trains running in multiple sections can be obtained by Equation (22), and other parameters can be attained by Equations (23)–(25).

$$u_r(x) = \sum_{i=1}^{N} \sum_{j=1}^{N} u_{rij}(x) \tag{22}$$

$$u_p(x) = \sum_{i=1}^{N} \sum_{j=1}^{N} u_{pij}(x) \tag{23}$$

$$i_r(x) = \sum_{i=1}^{N} \sum_{j=1}^{N} i_{rij}(x) \tag{24}$$

$$i_s(x) = \sum_{i=1}^{N} \sum_{j=1}^{N} i_{sij}(x) \tag{25}$$

Then, the distribution of rail potential and stray current can be simulated with multiple trains running in multiple sections at each moment.

The flow chart of simulation on rail potential dynamic distribution in this paper is shown in Figure 6. It mainly consists of four modules: the train movement calculation module, the power flow calculation module, the power flow tracing module and the rail potential module. Based on the route parameters, train characteristics, and scheduled timetables, the power and position of each train changing with time can be obtained by the train movement calculation module. At each time point, the segment of return circuit between traction substation and train is converted to lumped parameters. The voltage and current of each node in the network can be calculated by the power flow calculation module. For the nonlinear output characteristics of traction substations with RBEAD, the iterative method is usually used in power flow calculations. In each iteration, the operation state of the traction substation may change based on the catenary voltage. Based on the actual characteristic of the line, if more than one traction substation needs to change the operation state, only one traction substation is permitted to change the operation state in this iteration. The iteration will continue until the i-th step when the power-balance equations $\Delta P_n < \varepsilon_1$ and mismatch voltage of each node $\Delta U_n < \varepsilon_2$ are all fulfilled. Then, distribution of rail potential at this time point can be drawn by the power flow tracing module and rail potential module. The simulation will continue until the time exceeds the limit t_{end}. By this model, the dynamic distribution of the rail potential when multiple trains run in multiple sections with different train diagrams and line parameters can be simulated.

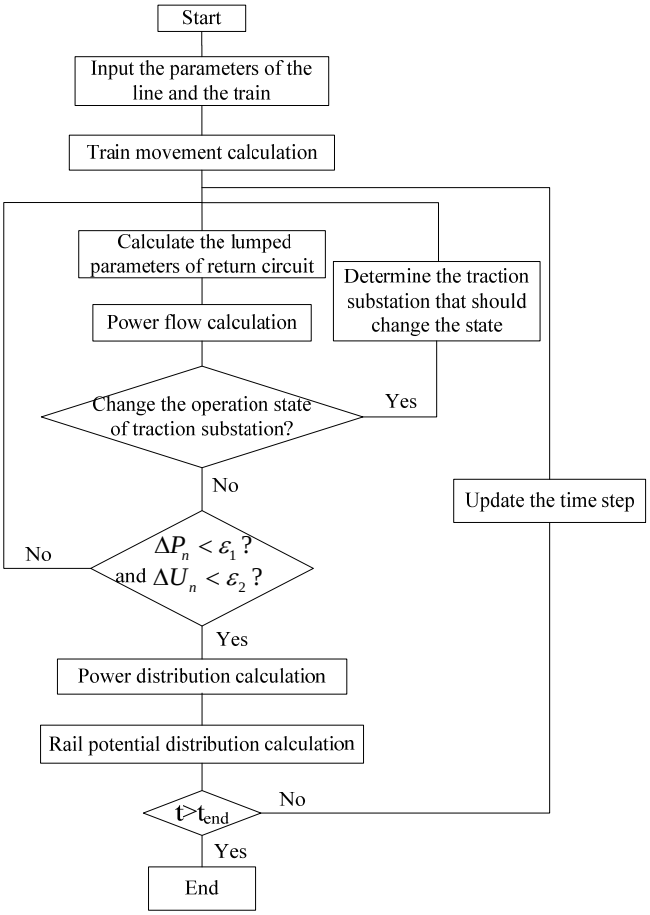

Figure 6. Flow chart of the simulation.

5. Simulation Results

Take the first-stage project of Guangzhou Metro Line 2 as an example to simulate the dynamic distribution of rail potential based on the method proposed in this paper. The parameters in the simulation are shown in Table 1.

Table 1. Simulation Parameters.

Parameter	Value
Equivalent resistance of the traction substation $y_{cN}/(\Omega)$	0.008
No-load voltage of the traction substation $U_0/(\mathrm{V})$	1593
Trigger voltage of regenerative braking energy absorbing device $U_{max}/(\mathrm{V})$	1800
Longitudinal resistance of the catenary $R_w/(\Omega/\mathrm{km})$	0.02
Longitudinal resistance of the running rail $R_r/(\Omega/\mathrm{km})$	0.02
Longitudinal resistance of the buried conductor $R_s/(\Omega/\mathrm{km})$	0.02
Longitudinal insulation conductance of rails to buried conductor $G_s/(\mathrm{S/km})$	1/15
Longitudinal insulation conductance of the buried conductor to the ground $G_p/(\mathrm{S/km})$	1/3
Mismatch power in the iteration $\xi_1/(\mathrm{kW})$	10^{-4}
Mismatch voltage of each node in the iteration $\xi_2/(\mathrm{V})$	10^{-4}

In the first-stage project of Guangzhou Metro Line 2, cross-bonding cables exist between the running rails of up line and down line. The catenaries of up line and down line are connected by positive buses at the position of traction substation, and they are independent in the interval. There are ten stations in the first-stage project of Guangzhou Metro Line 2. The locations of the stations are shown in Table 2.

Table 2. Locations of the Stations.

Station	Guangzhou Nan(S_1)	Shibi	Huijiang (S_2)	Nanpu	Luoxi (S_3)
Position/m	0	1020	3367	5800	6994
Station	Nanzhou	Dongxiao Nan(S_4)	Jiangtailu	Changgang	Jiangnan Xi(S_5)
Position/m	9387	10,291	12,265	13,171	14,042

Five traction substations, S_1 to S_5, are respectively set in Guangzhou Nan Station, Huijiang Station, Luoxi Station, Dongxiao Nan Station and Jiangnan Xi Station. Other stations are train stations without rectifier units and RBEAD. The train headway is 180 s in the up line and down line, and the dwell time of each train at each station is 30 s. The time step in the simulation is 0.5 s. In the simulation, the parameters of all trains in line are assumed to be the same. According to the operation characteristics of metro systems, the traffic will be regular from the time when the train diagram is stable. In the simulation, the train headway is 180 seconds in the up line and down line, and a train needs 1078 s to run from the departure station to the terminal station. There will be six trains at most in the whole line. Therefore, from the time of seventh train starting from the departure station, each 180 s demonstrate t cyclic behavior. Thus, the simulation can be carried out from 1080 s to 1260 s. In order to compare the current distribution in different situations, the simulation time in this paper is from 0 s to 1260 s.

The position-time curve of each train in the course of simulation is shown in Figure 7.

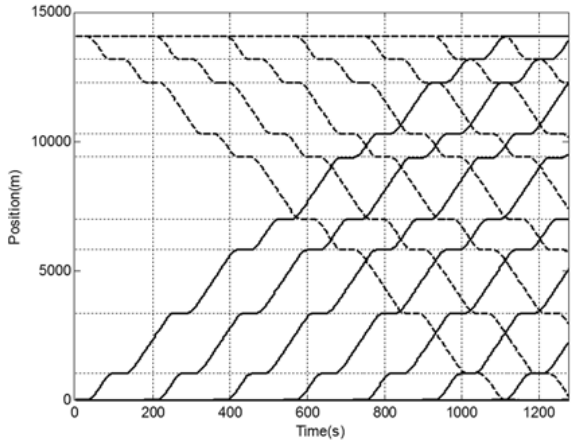

Figure 7. Train diagram in the simulation.

5.1. Model Validation

For the model validation, field tests of the rail potential were carried out on 16 August 2016, when two trains were tested in the line. In the field tests, two diagrams of the trains were used. In diagram 1, train 1 accelerated from Dongxiao Nan Station in the up line at 26 s, while train 2 accelerated from Nanpu Station in the down line at the same time. In diagram 2, train 1 accelerated from Dongxiao Nan Station in the up line at 0 s, and it began to brake at 38 s; train 2 accelerated from Nanpu Station in the down line at 26 s. The regenerative braking train was in high coincidence with the accelerating train in diagram 2. The simulation results comparing with field test results in two diagrams are shown in Figure 8. The field test point is set at Nanpu Station.

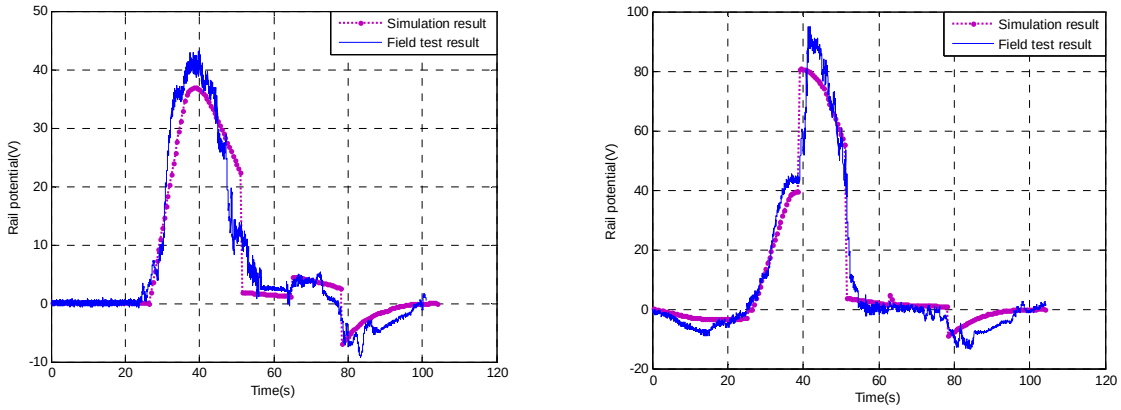

Figure 8. Simulation model validation, (**a**) Rail potential in diagram 1; (**b**) Rail potential in diagram 2.

As shown in Figure 8, the simulation results show the same trend with the field test results. The maximum value of the rail potential in field tests is higher than the simulation results. This situation may be caused by the increase of rail longitudinal resistance during the operation. In diagram 1, two trains accelerated at the same time. There is no regenerative braking current in the line, and the traction current of the train was supplied by the traction substations with a short distance. The maximum rail potential at Nanpu Station in the field test was 42.9 V. When the train in regenerative braking was in high coincidence with the accelerating train in diagram 2, the rail potential changed significantly. As shown in Fig. 8b, train 2 accelerated from Nanpu Station in the down line at 26 s. Train 1 in the up line began to brake at 38 s, and fed the regenerative energy back to the catenary. The maximum value of rail potential in the field test was 94.2 V, occurring at 42 s when train 1 was in regenerative braking. In diagram 2, the rail potential rose starkly when the accelerating train and regenerative braking train were in high coincidence. From the comparison of the simulation results and field test results, we can see that the simulation model can evaluate the rail potential effectively in the actual line.

5.2. Effect of Power Distribution on Rail Potential

During the simulation time, the dynamic distribution of the rail potential in the line is as shown in Figure 9.

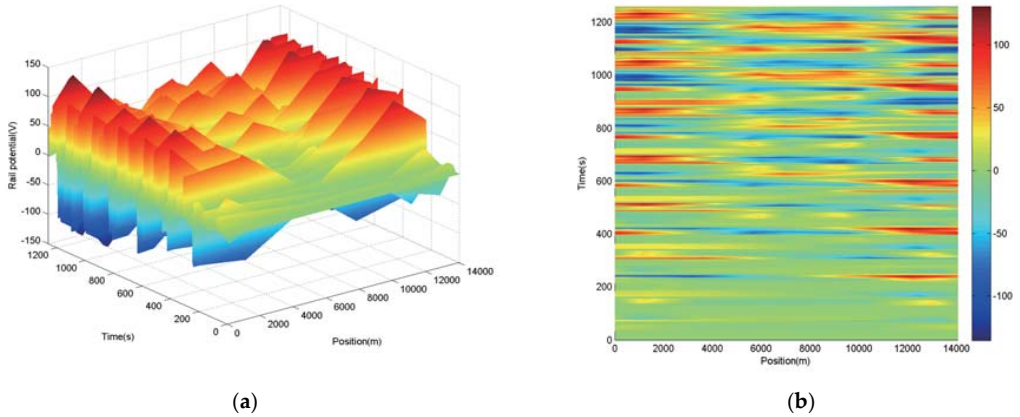

Figure 9. *Cont.*

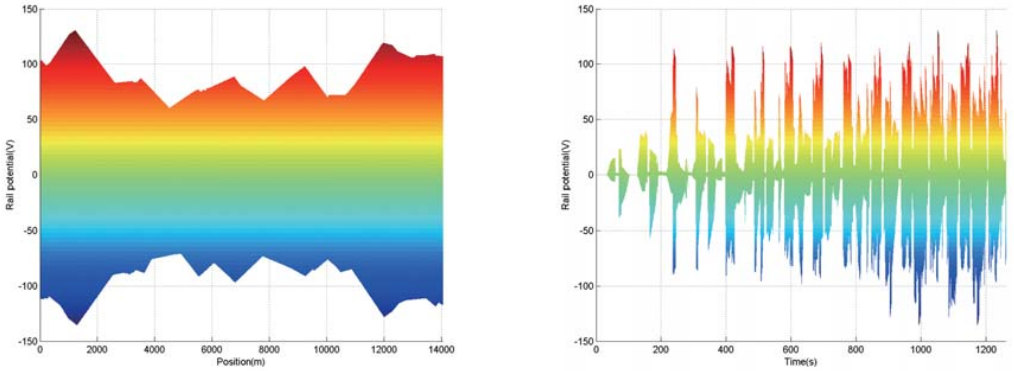

(**c**) (**d**)

Figure 9. Dynamic distribution of rail potential, (**a**) Dynamic distribution of rail potential; (**b**) Distribution of rail potential (time-position); (**c**) Distribution of rail potential (Rail potential-position); (**d**) Distribution of rail potential (rail potential-time).

As shown in Figure 9, a significant difference between rail potential exists in different times and positions. The maximum rail potential in the line is 130.8 V, occurring in 1230 m at 1231 s. As shown in Figure 9c, the simulation result of rail potential is consistent with the distribution in the actual line. The rail potential in the first and last sections is much higher than that in the middle sections during the operation of the line. The maximum and minimum values of the rail potential in each section and traction substation are shown in Table 3.

Table 3. Maximum and Minimum Rail Potential in Each Section and Traction Substation.

Position	S_1	Section1 (3367 m)	S_2	Section2 (3627 m)	S_3	Section3 (3297 m)	S_4	Section4 (3751 m)	S_5
Maximum (V)	103.3	130.8	83.7	88.6	80.6	98.0	72.3	119.3	107.3
Minimum (V)	−102.8	−135.2	−85.9	−96.7	−92.0	−92.0	−81.8	−127.9	−116.5

As clearly shown in Table 3, the rail potential in the first and last sections is higher than that in the middle sections. With the same parameters of the return circuit, the length of section 1 is 3367 m, and the maximum rail potential in section 1 is 130.8 V. By comparison, the length of section 2 is 3627 m, whereas the maximum rail potential is 88.6 V. From 1080 s to 1260 s, the maximum rail potential in section 1 is 130.8 V, occurring in 1230 m at 1231 s, and the maximum rail potential in section 2 is 88.6 V, occurring in 6756 m at 1178 s. Variation of the rail potential at typical moments and positions are shown in Figure 10.

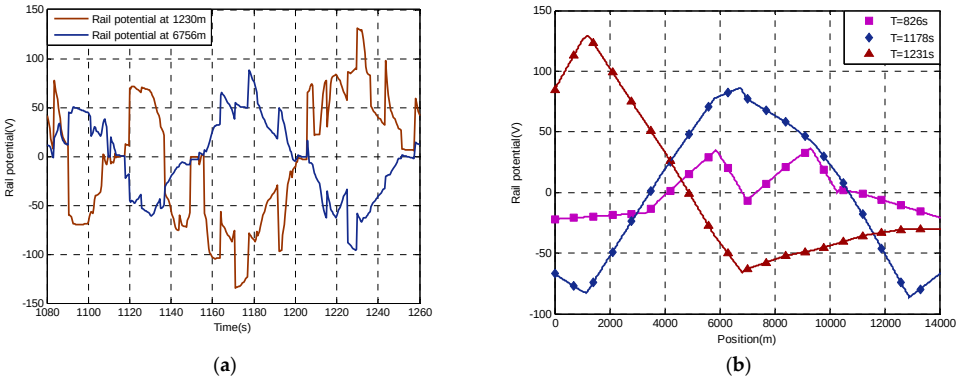

(**a**) (**b**)

Figure 10. Variation of the rail potential, (**a**) Variation of the rail potential at 1230 m and 6756 m; (**b**) Distribution of rail potential at three moments.

As shown in Figure 10a, at 1230s, the rail potential at the position of 1230 m is 89.3 V. When a train in section 2 begins regenerative braking at 1231 s, the rail potential reaches 130.8 V rapidly with the increase of the traction current transferring over the section. At 1177 s, the rail potential at 6756 m is 49.3 V. When a train in section 4 begins regenerative braking at 1178 s, the rail potential rises to 88.6 V with the increase of the traction current transferring over the section. During the period of the train in regenerative braking, the rail potential remains at a high level, and changes with the traction current transfers over the sections. It can be seen that rail potential is highly affected by the power distribution. As shown in Figure 10b, although the rail potentials at 1231 s and 1178 s are influenced by traction current transferring over sections, the maximum value in section 1 is much higher than that in section 2. Therefore, it is necessary to analyze the power distribution and rail potential at the two typical moments and positions. Meanwhile, the power distribution and rail potential at the time of 826 s is analyzed as a comparison. At 826 s, the total traction current is large, but there are no trains in regenerative braking in the line, and the traction current transferring over sections is low. The maximum rail potential in the line at 826 s is 35.3 V.

Table 4 shows the positions and current of all the trains and traction substations at 1231 s in the line.

As shown in Table 4, there are six trains, T_{u1}~T_{u6}, in the up line and there are six trains, T_{d1}~T_{d6}, in the down line at 1231 s. At this moment, T_{u2} and T_{d1} stop respectively at Huijiang Station and Changgang Station with a traction current of 0 A. Traction substations S_2, S_4 and S_5 are out of operation. The current distribution between the power sources and the loads are shown in Table 5.

As shown in Table 5, in the traction current of accelerating train T_{d6} at 1230 m, 1414.8 A comes from traction substation S_1 with the distance of 1230 m; 266.3 A comes from the regenerative braking train T_{u3} with the distance of 4571 m; 900.0 A comes from the regenerative braking train T_{d4} with the distance of 5598 m.

Table 6 shows the positions and current of all the trains and traction substations at 1178 s in the line.

Table 6 illustrates the current and positions of all trains and traction substations at 1178 s. At this moment, there are six trains, T_{u1}~T_{u6}, in the up line and there are six trains, T_{d1}~T_{d6}, in the down line. T_{d5} and T_{u6} stop respectively at Huijiang Station and Changgang Station; traction substations S_2 and S_4 are out of operation. The RBEAD at substations S_1 and S_5 are activated to absorb the remaining braking energy. The traction current distribution between the power sources and the loads are shown in Table 7.

As shown in Table 7, in the traction current of accelerating train T_{u3} at 6756 m, 147.7 A comes from the regenerative braking train T_{d6} with the distance of 5740 m, 538.9A comes from the regenerative braking train T_{u1} with the distance of 5592 m, 1073.2 A comes from the traction substation S_3 with the distance of 238 m, 609.3 A comes from the regenerative braking train T_{d1} with the distance of 6149 m.

Table 8 shows the positions and current of all the trains and traction substations at 826 s in the line.

Table 4. Positions and Current of the Trains and Traction Substations at 1231 Seconds.

Symbol	S_1	T_{u1}	T_{d6}	T_{u2}	S_2	T_{d5}	T_{u3}	T_{d4}	S_3	T_{u4}	T_{d3}	S_4	T_{u5}	T_{d2}	T_{u6}	T_{d1}	S_5
Current(A)	−2022.5	1187.2	2581.1	0	0	180.3	−398.6	−2349	444.2	167.4	−95.0	0	−35.4	169.8	170.5	0	0
Position(m)	0	1009	1230	3367	3367	4034	5801	6828	6994	8391	9383	10,291	10,293	11,274	12,821	13,171	14,042

Table 5. Current Distribution at 1231s.

Source	Load(A)							
	T_{u1}	T_{d6}	T_{d5}	S_3	T_{u4}	T_{d2}	T_{u6}	Total(A)
S_1	607.7	1414.8	0	0	0	0	0	2022.5
T_{u3}	132.3	266.3	0	0	0	0	0	398.6
T_{d4}	447.2	900.0	180.3	444.2	167.4	116.9	93	2349
T_{d3}	0	0	0	0	0	52.9	42.1	95
T_{u5}	0	0	0	0	0	0	35.4	35.4
Total(A)	1187.2	2581.1	180.3	444.2	167.4	169.8	170.5	

Table 6. Positions and Current of the Trains and Traction Substations at 1178 s.

Symbol	S_1	T_{d6}	T_{u1}	T_{d5}	S_2	T_{u2}	T_{d4}	T_{u3}	S_3	T_{d3}	T_{u4}	S_4	T_{d2}	T_{u5}	T_{d1}	T_{u6}	S_5
Current(A)	721.3	−387	-2133.6	0	0	178.2	1145.8	2369.1	−1214.5	184.8	615.5	0	359.9	173.7	−2879.7	0	866.5
Position(m)	0	1016	1164.0	3367	3367	3949	5808	6756	6994	8475	9390	10,291	10,294	11,189	12,905	13,171	14,042

Table 7. Current Distribution at 1178s.

Source	Load(A)									
	S_1	T_{u2}	T_{d4}	T_{u3}	T_{d3}	T_{u4}	T_{d2}	T_{u5}	S_5	Total(A)
T_{d6}	0	38.3	201	147.7	0	0	0	0	0	387
T_{u1}	721.3	139.9	733.5	538.9	0	0	0	0	0	2133.6
S_3	0	0	141.3	1073.2	0	0	0	0	0	1214.5
T_{d1}	0	0	70	609.3	184.8	615.5	359.9	173.7	866.5	2879.7
Total(A)	721.3	178.2	1145.8	2369.1	184.8	615.5	359.9	173.7	866.5	

Table 8. Positions and Current of the Trains and Traction Substations at 826 s.

Symbol	S_1	T_{d5}	T_{d4}	S_2	T_{u1}	T_{d3}	T_{u2}	S_3	T_{d2}	T_{u3}	S_4	T_{d1}	T_{u4}	T_{u5}	S_5
Current (A)	−82.2	0	0	−1105.7	189.7	2810.8	192.3	−2985.4	194.7	2696.8	−4207.4	2451.3	191.4	0	−346.3
Position (m)	0	1020	3367	3367	3771	5886	6581	6994	8653	9330	10,291	10,345	11,011	13,168	14,042

Table 8 illustrates the current and positions of all trains and traction substations at 826 s. At this moment, the maximum rail potential in the line is 35.3 V. There are five trains T_{u1}~T_{u5} in the up line and five trains, T_{d1}~T_{d5}, exist in the down line. T_{d5}, T_{d4} and T_{u5} stop respectively in Shibi Station, Huijiang Station, and Changgang Station. The current distribution between the power sources and the loads are shown in Table 9.

Table 9. Current Distribution at 826 s.

Source	Load (A)							
	T_{u1}	T_{d3}	T_{u2}	T_{d2}	T_{u3}	T_{d1}	T_{u4}	Total (A)
S_1	13.1	64.2	4.9	0	0	0	0	82.2
S_2	176.6	863.8	65.3	0	0	0	0	1105.7
S_3	0	1882.8	122.1	145.8	834.7	0	0	2985.4
S_4	0	0	0	48.9	1862.1	2279	17.4	4207.4
S_5	0	0	0	0	0	172.3	174	346.3
Total(A)	189.7	2810.8	192.3	194.7	2696.8	2451.3	191.4	

As shown in Table 9, the total traction current of all the accelerating trains in line is 8727.2 A, whereas the total traction current is respectively 4456.3 A at 1231 s and 5027 A at 1178 s. However, the maximum rail potential at 826s is much lower than that at 1231 s and 1178 s. Although the total traction current is high at 826 s, there are no regenerative braking trains in the line at this moment. The traction current of accelerating trains comes from the traction substations with a short distance. In the traction current of the accelerating train T_{d3} at 5886 m, 1882.8 A comes from the traction substation S_3 with the distance of 1108 m; 863.8 A comes from the traction substation S_2 with the distance of 2519 m; and 64.2 A comes from S_1 with the distance of 5886 m. In the traction current of the accelerating train T_{u3} at 5933 m, 834.7 A comes from the traction substation S_3 with the distance of 2336 m; and 1862.1 A comes from the traction substation S_4 with the distance of 961 m. In the traction current of the accelerating train T_{d1} at 10,345 m, 2279 A comes from the traction substation S_4 with the distance of 54 m, and 172.3 A comes from the traction substation S_5 with the distance of 3697 m.

Comparing the distribution of traction current and rail potential at 826 s, 1178 s and 1231 s, we know that rail potential will increase abnormally when regenerative braking trains feed current back to the catenary and the current is absorbed by the accelerating trains at long distance.

Based on the distribution of traction current and rail potential, the mechanism that rail potential in the first and last sections is much higher than that in the middle sections is analyzed. Maximum rail potential in section 1 is 130.8 V, occurring at 1231 s at the position of T_{d6}, 42.2 V higher than that in section 2, occurring in 1178 s at the position of T_{u3}. In this paper, transmission distance of traction current (*TDTC*) is proposed to describe the transmission distance of the load's traction current at node j. $TDTC = \sum_{i=1}^{N} I_{ij} \times |x_i - x_j|$. The *TDTC* of T_{d6} is 7996.6 A·km at 1231 s, and the *TDTC* of T_{u3} is 7863.3 A·km at 1178 s. There is little difference between the *TDTC* of the two trains, but rail potential in the position of T_{d6} is much higher than that in the position of T_{u3}. Comparing the *TDTCs*, we find that unilateral nature of the T_{d6} is more obvious: 1740.2 A·km of the *TDTC* comes from the power sources in the section of 0 m to T_{d6}, whereas 6256.4 A·km of the *TDTC* comes from the power sources in the section of T_{d6} to L. The *TDTC* of T_{u3} is relatively bilateral at 1178 s; 3861.3 A·km of the *TDTC* comes from the power sources in the section of 0 m to T_{u3}; 4002 A·km) of the *TDTC* comes from the power sources in the section of T_{u3} to L. Therefore, the rail potential with multiple trains running in multiple sections is influenced by the *TDTC* and the unilateral nature or bilateral nature of the train's traction current.

When the system is in dynamic operation, there are multiple trains in the line. If the current that the regenerative braking train feed backs to the catenary is absorbed by the accelerating trains at long distance, then the rail potential may rise abnormally. The traditional methods such as shortening

the distance between traction substations or ensuring the longitudinal resistance within the standard values cannot control the rail potential effectively.

5.3. An Analysis of Stray Current

An analysis of stray current when multiple trains run in multiple sections is carried out in this paper. The simulation result of the buried conductor potential is shown in Figure 11, and the simulation result of the stray current in the buried conductor is shown in Figure 12.

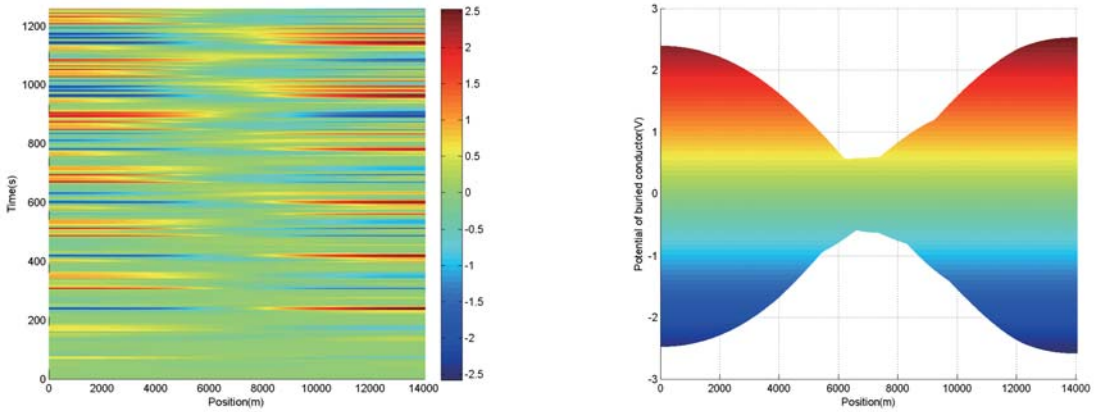

(**a**) (**b**)

Figure 11. Distribution of buried conductor potential, (**a**) Distribution of buried conductor potential (time-position); (**b**) Distribution of buried conductor potential (potential-position).

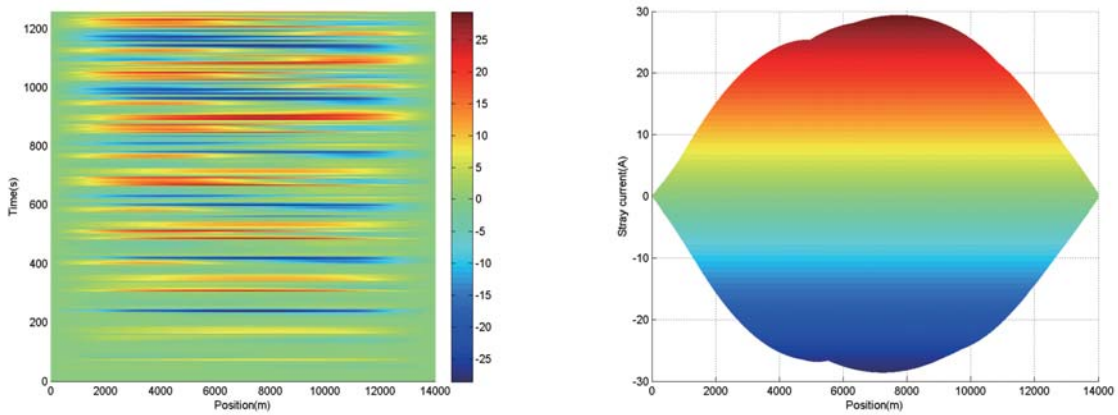

(**a**) (**b**)

Figure 12. Distribution of stray current, (**a**) Distribution of stray current (time-position); (**b**) Distribution of stray current (stray current-position).

As shown in Figure 11, influenced by the distribution of rail potential, the buried conductor potential in the first and last sections is much higher than that in the middle sections. The maximum buried conductor potential is 2.36 V, occurring in 238 s at 14,042 m. The minimum buried conductor potential is −2.42 V, occurring at 1084 s in 14,042 m. The maximum and minimum buried conductor potentials have exceeded the standard limits. Figure 13a illustrates the buried conductor potential at 826 s, 1178 s and 1231 s. Although the total traction current at 826 s is much higher than that at 1178 s and 1231 s, the maximum buried conductor potential is 0.18 V at 826 s, and the maximum buried conductor potentials at 1178 s and 1231 s are 0.56 V and 2.06 V, respectively. The buried conductor potential is highly affected by the power distribution.

Figure 12 illustrates the distribution of stray current in buried conductor. Stray current is low at both ends of the line, and is high in the middle sections. The maximum positive stray current in the buried conductor is 29.39 A, occurring in 904 s at 7760 m. The maximum negative stray current in the buried conductor is 28.59 A, occurring in 238 s at 7230 m. The distribution of stray current at 826 s, 1178 s and 1231 s is shown in Figure 13b. Maximum stray current in buried conductor at 826 s, 1178 s and 1231 s are 4.63 A, 12.13 A, and 25.41 A respectively. Stray current is highly affected by the power distribution.

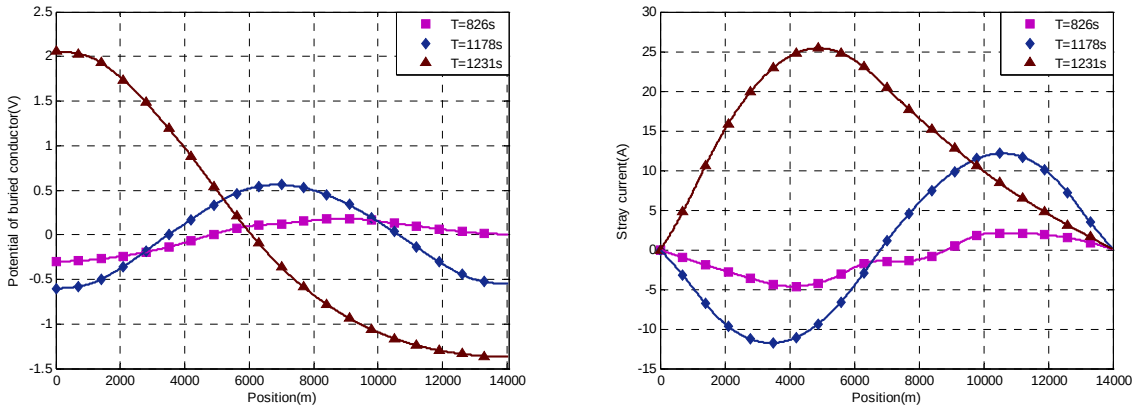

(**a**) (**b**)

Figure 13. Comparison of buried conductor potential and stray current at three moments, (**a**) Distribution of buried conductor potential at three moments; (**b**) Distribution of stray current at three moments.

6. Summary and Conclusion

In this paper, a dynamic simulation model for evaluation of the rail potential when multiple trains run in multiple sections is presented, and the impact of power distribution on abnormal rise of rail potential is analyzed. With the simulation model in this paper, the distribution of rail potential in the dynamic operation of the line can be simulated rapidly and accurately. Conclusions can be drawn as follows:

(1) A dynamic simulation model for evaluation of the rail potential is proposed in this paper. The model incorporates train movement calculation, power flow calculation, power flow tracing and rail potential calculation. For realization of fast and accurate calculation, return circuit is converted to lumped parameters in power flow calculation and is modeled with distributed parameters in rail potential calculation. Based on this model, the impact of power distribution on rail potential in dynamic operation of the system can be analyzed effectively.

(2) Traction current transferring over sections widely exists in DC traction power systems when multiple trains run in multiple sections. The power flow tracing method proposed in this paper can obtain the power distribution between power sources and loads effectively.

(3) Rail potential and stray current is highly affected by the power distribution. When the traction current transferring over sections increases, rail potential and stray current are relatively high. Rail potential with multiple trains running in multiple sections is also influenced by the unilateral nature or bilateral nature of the train's traction current.

Acknowledgments: This work is supported by the National Natural Science Foundation of China (Grant No. 51147011), the Jiangsu Provincial Natural Science Foundation of China (Grant No. BK20130187), and the Research and Innovation Program of Postgraduates of Jiangsu Province (KYLX 1383).

Author Contributions: Guifu Du wrote the paper and designed the simulation model; Dongliang Zhang contributed to the conception of the study and provided the line and vehicle data; Guoxin Li analyzed the power distribution of DC traction power systems; Chonglin Wang analyzed the simulation data; Jianhua Liu helped to perform the analysis with constructive discussions.

Conflicts of Interest: The authors declare no conflict of interest

References

1. Ogunsola, A.; Sandrolini, L.; Mariscotti, A. Evaluation of Stray Current From a DC-Electrified Railway with Integrated Electric–Electromechanical Modeling and Traffic Simulation. *IEEE Trans. Ind. Appl.* **2015**, *51*, 5431–5441. [CrossRef]
2. Railway Applications-Fixed Installations-Electrical Safety, Earthing and the Return Circuit-Part 2: Provisions Against the Effects of Stray Currents Caused by D.C. Traction Systems. Available online: http://standards.globalspec.com/std/1316409/ds-en-50122-2 (accessed on 26 June 2016).
3. Railway Applications-Fixed Installations-Electrical Safety, Earthing and the Return Circuit-Part 1: Protective provisions against electric shock. Available online: http://standards.globalspec.com/std/9987312/cenelec-en-50122-1 (accessed on 28 June 2016).
4. Yang, C.; Cui, G.; Li, Z.; Zhao, Y.; Zhang, C. Study the Influence of DC Stray Current on the Corrosion of X65 Steel Using Electrochemical Method. *Int. J. Electrochem. Sci.* **2015**, *10*, 10223–10231.
5. Dolara, A.; Foiadelli, F.; Leva, S. Stray Current Effects Mitigation in Subway Tunnels. *IEEE Trans. Power Deliv.* **2012**, *27*, 2304–2311. [CrossRef]
6. Sanchez-Sutil, F.; Hernández, J.C.; Tobajas, C. Overview of electrical protection requirements for integration of a smart DC node with bidirectional electric vehicle charging stations into existing AC and DC railway grids. *Electr. Power Syst. Res.* **2015**, *122*, 104–118. [CrossRef]
7. Hernandez, J.C.; Sutil, F.S.; Vidal, P.G. Protection of a multiterminal DC compact node feeding electric vehicles on electric railway systems, secondary distribution networks, and PV systems. *Turk. J. Electr. Eng. Comp. Sci.* **2016**, *24*, 3123–3143. [CrossRef]
8. Chen, S.L.; Hsu, S.C.; Tseng, C.T.; Yan, K.H.; Chou, H.Y.; Too, T.M. Analysis of Rail Potential and Stray Current for Taipei Metro. *IEEE Trans. Veh. Technol.* **2006**, *55*, 67–75. [CrossRef]
9. Tzeng, Y.; Lee, C. Analysis of Rail Potential and Stray Currents in a Direct-Current Transit System. *IEEE Trans. Power Deliv.* **2010**, *25*, 1516–1525. [CrossRef]
10. Lee, C.H.; Lu, C.J. Assessment of Grounding Schemes on Rail Potential and Stray Currents in a DC Transit System. *IEEE Trans. Power Deliv.* **2006**, *21*, 1941–1947. [CrossRef]
11. Xu, S.; Li, W.; Wang, Y. Effects of Vehicle Running Mode on Rail Potential and Stray Current in DC Mass Transit Systems. *IEEE Trans. Veh. Technol.* **2013**, *62*, 3569–3580.
12. Charalambous, C.A.; Cotton, I.; Aylott, P. Modeling for Preliminary Stray Current Design Assessments: The Effect of Crosstrack Regeneration Supply. *IEEE Trans. Power Deliv.* **2013**, *28*, 1899–1908. [CrossRef]
13. Charalambous, C.A.; Aylott, P. Dynamic Stray Current Evaluations on Cut-and-Cover Sections of DC Metro Systems. *IEEE Trans. Veh. Technol.* **2014**, *63*, 3530–3538. [CrossRef]
14. Pires, C.L.; Nabeta, S.I.; Cardoso, J.R. ICCG method applied to solve DC traction load flow including earthing models. *IET Electr. Power Appl.* **2007**, *1*, 193–198. [CrossRef]
15. Zaboli, A.; Vahidi, B.; Yousefi, S.; Hosseini-Biyouki, M.M. Evaluation and Control of Stray Current in DC-Electrified Railway Systems. *IEEE Trans. Veh. Technol.* **2016**. [CrossRef]
16. Lin, F.; Liu, S.; Yang, Z.; Zhao, Y.; Yang, Z.; Sun, H. Multi-Train Energy Saving for Maximum Usage of Regenerative Energy by Dwell Time Optimization in Urban Rail Transit Using Genetic Algorithm. *Energies* **2016**, *9*. [CrossRef]
17. Falvo, M.C.; Sbordone, D.; Fernandez-Cardador, A.; Cucala, A.P.; Pecharroman, R.R.; Lopez-Lopez, A. Energy savings in metro-transit systems: A Comparison Between Operational Italian and Spanish lines. *J. Rail Rapid Transit.* **2014**, *230*, 345–359. [CrossRef]
18. Arboleya, P.; Coto, M.; González-Morán, C.; Arregui, R. On board accumulator model for power flow studies in DC traction networks. *Electr. Power Syst. Res.* **2014**, *116*, 266–275. [CrossRef]
19. Coto, M.; Arboleya, P.; Gonzalez-Moran, C. Optimization approach to unified AC/DC power flow applied to traction systems with catenary voltage constraints. *Int. J. Electr. Power Energy Syst.* **2013**, *53*, 434–441. [CrossRef]

20. Xia, H.; Chen, H.; Yang, Z.; Lin, F.; Wang, B. Optimal Energy Management, Location and Size for Stationary Energy Storage System in a Metro Line Based on Genetic Algorithm. *Energies* **2015**, *8*, 11618–11640. [CrossRef]
21. Lee, H.M.; Jeong, E.J.; Jeong, S.C. A Study on Calculation of DC Railway Loadflow with Energy Storage System. *ICCAS* **2010**, *10*, 800–803.
22. Silva, J.A.P.; Cardoso, J.R.; Rossi, L.N. A Fourth Order Differential-Integral Formulation Applied to the Simulation of the Subway Grounding Systems. *Electr. Power Compon. Syst.* **2002**, *30*, 331–343. [CrossRef]